IOP Publishing Journal of Physics: Condensed Matter
J. Phys.: Condens. Matter **31** (2019) 223001 (12pp) https://doi.org/10.1088/1361-648X/ab0bf4

Topical Review

Charge and spin transport on surfaces and atomic layers measured by multi-probe techniques

Shuji Hasegawa

School of Science, University of Tokyo, Hongo 7-3-1, Bunkyo-ku, Tokyo 113-0033, Japan

E-mail: shuji@surface.phys.s.u-tokyo.ac.jp

Received 27 November 2018, revised 31 January 2019
Accepted for publication 1 March 2019
Published 26 March 2019

Abstract

Thanks to advances in *in situ* measurement techniques for electrical transport in ultra-high vacuum together with emergent materials such as Rashba-type surfaces, topological insulators, atomic-layer superconductors, and 2D materials like graphene, surface states and edge states on crystals provide intriguing topics, e.g. dissipation-less currents, spin-polarized electric current, and pure spin current. This is due to broken symmetry and strong spin–orbit and electron–phonon interactions. Here we review some examples of experimental techniques of multi-probe methods at macroscopic and microscopic scales, followed by transport phenomena revealed by them. These are opening a field in condensed matter physics driven by symmetry breaking at surfaces and atomic layers.

Keywords: surface-state transport, atomic-layer superconductors, Rashba effect, topological insulators, spin current

(Some figures may appear in colour only in the online journal)

1. Introduction

Since lateral electrical conduction through electronic states at crystal surfaces, so-called *surface-state transport*, is now detected directly [1–4], intriguing phenomena have been found in it, such as atomic-layer superconductivity, spin-polarized electrical current, and pure spin current at Rashba/topological surface states and two-dimensional (2D) materials such as graphene and its intercalation compounds [5–8]. This is owing to recent advances in experimental techniques of *in situ* multi-probe transport measurements in ultra-high vacuum (UHV). This should be contrasted to vertical electrical conduction at surfaces/interfaces where energy barriers such as tunneling barrier, Schottky barrier and pn junction play main roles in observed phenomena. The lateral transport along the topmost surface of crystals has been a new branch of surface science emerging in the last decades. Due to, e.g. spin-momentum locking effect at Fermi surfaces, helical/chiral edges states, (inverse) spin Hall effect, (inverse) Edelstein effect, and so on, electrical conduction at surfaces/interfaces is non-trivial and non-reciprocal where the direction of charge/spin propagation and spin polarization of current are controlled by some quantum mechanisms. These phenomena are universally observed at crystal surfaces, interfaces, and atomic layers where space-inversion symmetry is broken down. In this point of view, surface and interfaces of materials are an important platform for rich physics.

In this short review, after outlining the multi-probe techniques in UHV, including electrode pads fabricated on sample surfaces, detachable monolithic multi-probes, and four-tip scanning tunneling microscope (STM), some examples of transport phenomena revealed by the methods are introduced, which are found on surface superstructures, Rashba-type surface systems, graphene, transition-metal dichalcogenides, atomic-layer superconductors, and topological insulators. These results may lead to some impact on condensed matter

physics such as unconventional superconductivity and applications to nano-electronics and spintronics.

2. *In situ* measurements techniques

Many of surfaces and atomic-layer materials are easily oxidized and deteriorated when they are taken out of UHV chambers where the samples are grown and prepared. Therefore, it is indispensable to measure their transport properties *in situ* in UHV without exposing the samples to air. On the other hand, we often need high-temperature heating and material deposition/growth at elevated temperatures to prepare the clean surfaces and atomically well-defined materials in UHV. Therefore, for electrical transport measurements of such samples, we need multi-electrodes which are compatible with such UHV heating processes or electrodes detached during such sample preparations. It is, however, not easy to put such multi-electrodes on the samples in UHV.

Four-terminal measurements of electrical resistance are indispensable for surfaces and nanostructures where their electrical resistance is comparable to the contact resistance at the terminals/probes contacts. Two-terminal measurements, therefore, are useless where the contact resistance is inevitably involved in the measured results. Therefore, we need four-probe methods in which two of the four are for current source and other two are for measuring the voltage drop.

As shown in figure 1, researchers have developed several kinds of such electrodes. One of them is fixed electrodes (contact pads) fabricated in advance on the sample surface which are made of materials (e.g. Ta- and W-silicide on Si crystals) compatible with the high-temperature heating in UHV (figure 1(a)) [9]. In other cases, the electrodes are fabricated, by metal deposition and/or area-selecting sputtering with a mask on the sample surface after preparing the aimed sample structures (figure 1(b)) [11]. Figure 1(c) shows a simple method for four-terminal resistance measurements where two thin Ta or W wires are just pressed down on the sample surface for voltage measurement while the clamps at both ends of sample are for current source [10]. The wires always contact the sample surface even during the heat treatments. Figure 1(d) shows a method where fixed electrodes are fabricated on the sides of sample crystal in advance which are used for measurements after cleaving the crystal in UHV to expose the flesh surface [13, 14]. These macroscopic electrodes for four-terminal resistance measurements are fixed on the sample in advance.

Other methods are multi-probes which are retracted from the sample during the sample preparation and are then in contact with sample for transport measurements (figures 1(e)–(g)) [12, 15, 16]. Such multi-probe methods contain monolithic types (figures 1(e) and (f)) where the probes are fixed with each other [12, 15], and multi-tip prober types (figure 1(g)) where the probe spacing and arrangement can be changed arbitrarily [16, 17].

Furthermore, it has been now possible in the last decade to carry out the *in situ* transport measurements in UHV at very low temperatures (less than 1 K) under strong magnetic field (up to around 10 T) [18, 19]. These UHV machines are based on low-temperature STM techniques under magnetic field. These developments in the experimental techniques have been indispensable for research of surfaces and atomic-layer materials.

In addition to four-probe resistance measurements, scanning tunneling potentiometry (STP), as shown schematically in figure 2(a), is also useful to measure electrical resistance at nanometer scales by using multi-tip STM [5, 20, 21, 22]. In STP, by electrical current fed through the outer pair of tips, potential gradient occurs along the sample surface, which is measured by the third tip in scanning tunneling spectroscopy (STS) mode; the tunneling bias for the third tip is adjusted so that the tunneling current through the tip is zero at each point on the sample surface. By mapping the tunneling bias voltage at each point on the surface, this method enables us to visualize the potential distribution caused by the current, and to correlate it with the atomic-scale structures such as atomic steps and domain boundaries on the surface. Actually the STP have revealed resistance at atomic steps on graphene [5] and Si(1 1 1)- $\sqrt{3} \times \sqrt{3}$-Ag surfaces [20–22]. Figure 2(b) shows an example of STP measurements on a surface of a topological insulator [23]; the potential distribution caused by the lateral current across the surface is shown in color code, overlapped on a topographic terrain obtained simultaneously by STM mode. Potential drops at step edges as well as a continuous potential gradient on terraces are observed, as reported by previous paper [24]. An interesting finding is potential drops at domain boundaries (indicated by a yellow arrow) which is much larger than that at the steps. A void on the surface shows a dipole-like feature in the potential distribution as shown in figure 2(c) [23]. STP will expand its versatile usability when magnetic tips are used as the third tip for measuring spin-resolved transport [25, 26].

3. Surface-state transport

The first example shown here for four-probe resistance measurements in UHV is surface-state transport at Indium-adsorbed Si(1 1 1) surfaces. It is known that, depending on the adsorption amount of Indium at monolayer (ML) regime, various kinds of surface superstructures are formed on Si(1 1 1) substrate [1]; $\sqrt{3} \times \sqrt{3}$ structure at 1/3 ML, $\sqrt{31} \times \sqrt{31}$ structure at 0.55(=17/31) ML [27], 4×1 structre at 1 ML, and $\sqrt{7} \times \sqrt{3}$ structur at 2 ML [40] coverages of In, respectively. At the $\sqrt{3} \times \sqrt{3}$ and $\sqrt{31} \times \sqrt{31}$ structures (figures 3(a)–(d)), Indium atoms saturate dangling bonds of the Si substrate and they are away from each other, resulting in insulating (semiconducting) band structures. At the 4×1 structure (figures 3(e) and (f)), Indium atoms periodically arrange themselve densely in a particular crystal orientation on the surfae to make a stripe pattern, so that it makes a quasi-1D metallic band structure along the Indium atomic chains [28, 29]. The $\sqrt{7} \times \sqrt{3}$ structure has an isotropic metallic and 2D free-electron-like band structure [30], revealed by angle-resolved photoemission spectroscopy (ARPES).

As shown in figure 3(i) [31], the sheet resistivity of the respective surface structures was measured *in situ* by the monolithic micro-four-point probe (micro-4PP) (figure 1(e)) in a UHV chamber [32]. It is interesting to see that the resistivity

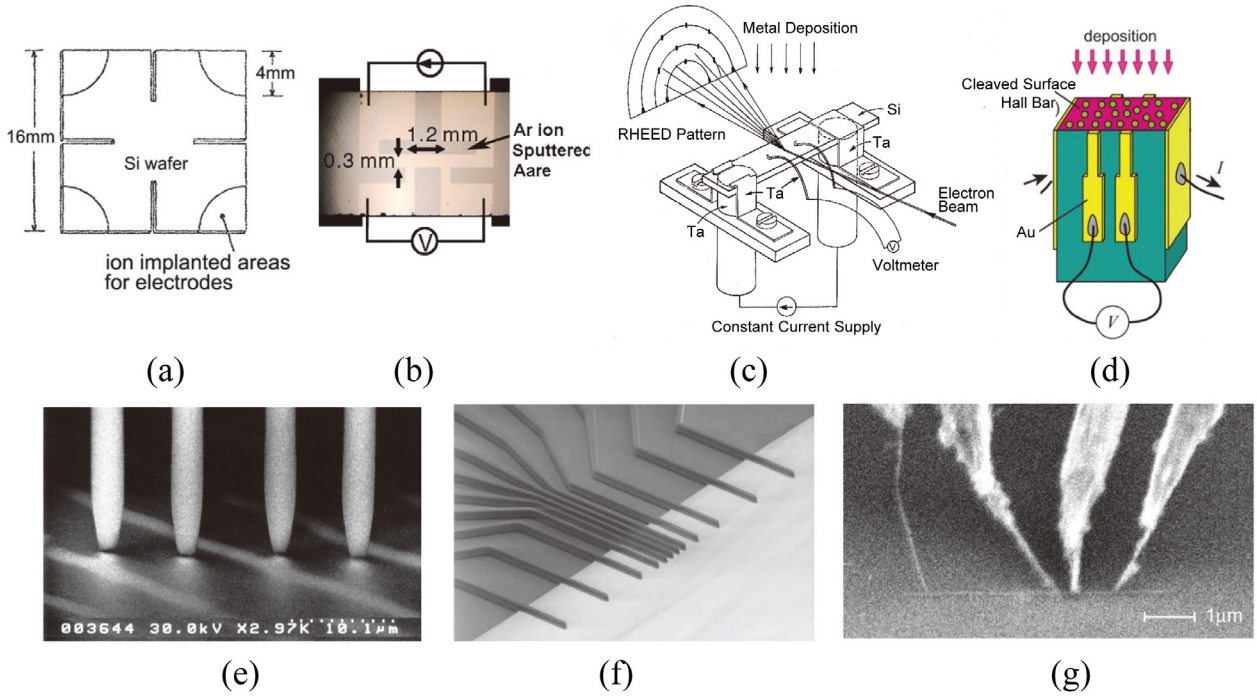

Figure 1. Various kinds of electrodes for *in situ* four-terminal conductivity measurements which are compatible with high-temperature treatments of samples in UHV. (a) Silicide electrodes for van der Pauw method, formed by ion implantation before UHV installation. Reprinted from [9], with the permission of AIP Publishing. (b) Patterning by Ar^+ sputtering after sample preparation. Reproduced from [11], CC BY 2.0. (c) Ta-wire contacts pressed on the sample. Reprinted figure with permission from [10], © 1992 by the American Physical Society. (d) Cleavage of a sample crystal together with electrodes attached on the sides of crystal. Reprinted from [13], with the permission of AIP Publishing. (e) Monolithic micro-four-point probe (reproduced with permission from [12]. Copyright @ World Scientific) and (f) twelve-point probe. Reprinted from [15], with the permission of AIP Publishing. (g) Independently-driven four-tip STM with carbon nanotube tips. Reprinted with permission from [16]. Copyright © 2007 American Chemical Society.

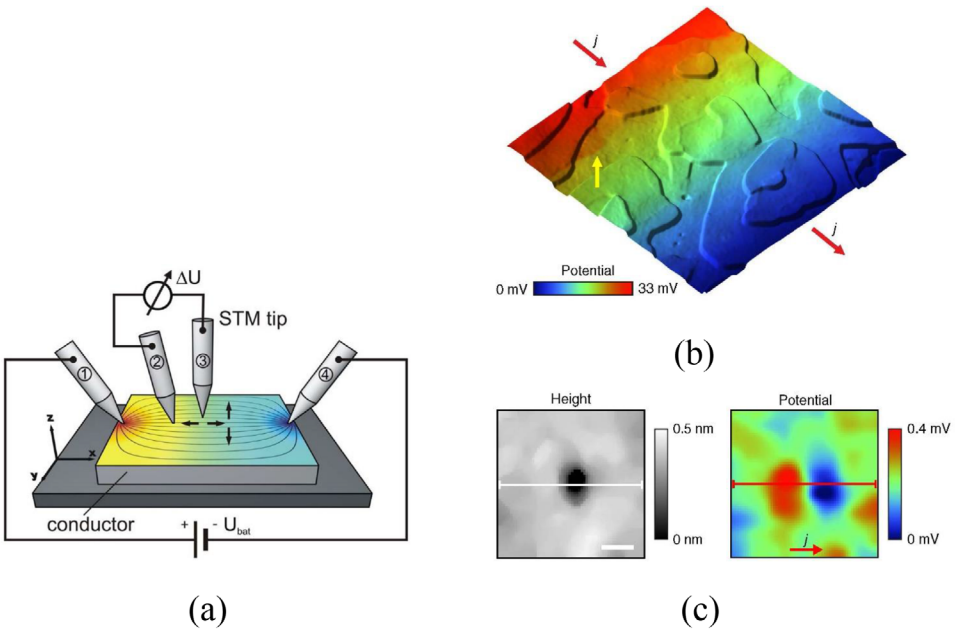

Figure 2. (a) Schematic of scanning tunneling potentiometry (STP) using multi-tip STM. Reprinted from [20], with the permission of AIP Publishing. Tip ① and tip ④ are for current injection. Tip ③ is for STM scanning to obtain topography and potential distribution with respect to Tip ②. (b) An example of STP measurements on a topological insulator $(Bi_{1-x}Sb_x)_2Te_3$ surface. The potential distribution, shown by color code, is overlapped on the topographic terrain of the surface. The scan size is 300 nm. (c) STM image (left) of a void on the same surface, and the corresponding potential map (right) showing a dipole shaped feature centered at the void. The scale bar is 5 nm. Reproduced from [23], CC BY 4.0.

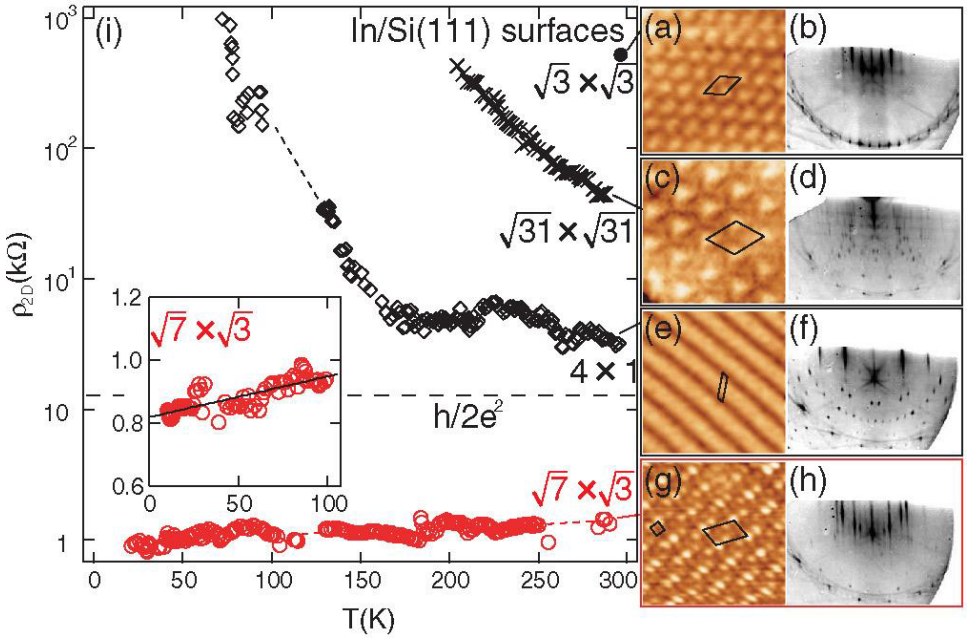

Figure 3. (a)–(h) are STM images and reflection-high-energy electron diffraction (RHEED) patterns of the $\sqrt{3} \times \sqrt{3}$, $\sqrt{31} \times \sqrt{31}$, 4×1, $\sqrt{7} \times \sqrt{3}$ surface superstructures, respectively. (i) Measured sheet resistivity (ρ_{2D}) plotted on a logarithmic scale as a function of temperature for the In/Si(1 1 1) surfaces: the $\sqrt{3} \times \sqrt{3}$ (filled circles), $\sqrt{31} \times \sqrt{31}$ (crosses), 4×1 (open diamonds), and $\sqrt{7} \times \sqrt{3}$ (open circles). Reprinted figure with permission from [31], © 2011 American Physical Society. The horizontal broken line indicates the inverse of the minimum metallic conductivity. The inset shows a magnified figure of the measured sheet resistivity for the $\sqrt{7} \times \sqrt{3}$ surface at low temperatures.

differs by several orders of magneitudes at room temperature (RT) depending on the surface superstructures. This indicates high sensitivity to the surface transport in micro-4PP measurements (8 μm probe-spacing). Furthermore, the temperature dependence of resistivity is also different from each other. The resistivity of the $\sqrt{31} \times \sqrt{31}$ (and $\sqrt{3} \times \sqrt{3}$)) surface increases monotonically with cooling, showing an insulating character, consistent with the surface-band structure. The 4×1 surface shows a metal-to-insulator transition around 130 K, characteristic to quasi-1D metallic systems [29, 33]; the resistance increases steeply below ca. 130 K while it remains almost constant above 130 K. Only the $\sqrt{7} \times \sqrt{3}$ surface shows a metallic behavior, showing a decarese in resistance with cooling. This surface shows superconductivity with further cooling as described below.

Since the surface states are 2D electronic systems of about one-atom-layer thick, they should have large fluctuation and should not have any phases with long-range order at low temperatures according to Mermin–Wargner Theorem. Therefore, it had been thought that supercondutivity should not occur in the surface states. In fact, even by a report that low-temperature STS showed superconducting energy-gap opening at surface structures of Si(1 1 1) covered by one or two atomic layers of In and Pb [34], people believed that the superconductivity probed by STS was very local and it should not be globally coherent superconductivity. It should be based on the Berezinskii–Kosterlitz–Thouless mechanism [35].

After that, however, Uchihashi *et al* detected superconducting current through the surface states between millimeter-apart electrodes (shown in figure 1(b)). This confirmed the 'surface-state superconductivity' with long-range coherency [36]. This is due to the finite thickness of the surface state, a quasi-2D system, which, then, can have a long-range order; the wavefunction of surface sates extends by several atomic layers deep below the surface, and the Cooper pair wavefunction is coherent in macroscopic scale (though the superconducting fluctuation is large compared with 3D superconductivity).

Figure 4(a) shows the temperature dependence of the sheet resistivity of Si(1 1 1)- $\sqrt{7} \times \sqrt{3}$-In surface [37] measured by the monolithic micro-4PP (figure 1(e)) working at sub-Kelvin temperature under strong magnetic field in UHV [18]. It shows a superconducting transition around 2.8 K though it is not a sharp transition compared to bulk superconductors; the resistance gradually decreases well above the critical temperature. This is due to large superconducting fluctuation, intrinic to low-dimensional systems. Actualy this gradual transition is well reproduced by Aslamazov–Larkin and Maki–Thompson corrections for the 2D cases [37].

Figure 4(b) shows change in the sheet resistivity at 0.8 K as a fucntin of the magnetic field applied perpendicular to this surface [37]. The superconductivity is broken around 0.4 T. This is the upper critical field H_{C2}, of which temperature dependence gives us the Ginzburg–Landau (GL) coherence length ξ_{GL}, $\xi_{GL} = 25 \pm 7$ nm [37]. On the other hand, the Pippard coference length ξ, which is derived from the band parameters obatined by ARPES and STS measurements, is 610 nm, much longer than ξ_{GL}. This is due to the influnece of a short mean free path of carriers λ by a relation $1/\xi_{GL} = 1/\xi + 1/\lambda$, meaning $\lambda \approx \xi_{GL}$ in this system, i.e. a so-called dirty superconductor. The short λ may come from defects on the surface as well as the large fluctuation.

It is also known that adorption of Pb around monolayer regime coverages on Si(1 1 1) induces various kinds of surface phases [38, 39]. A hexagonal incommensurate (HIC) phase

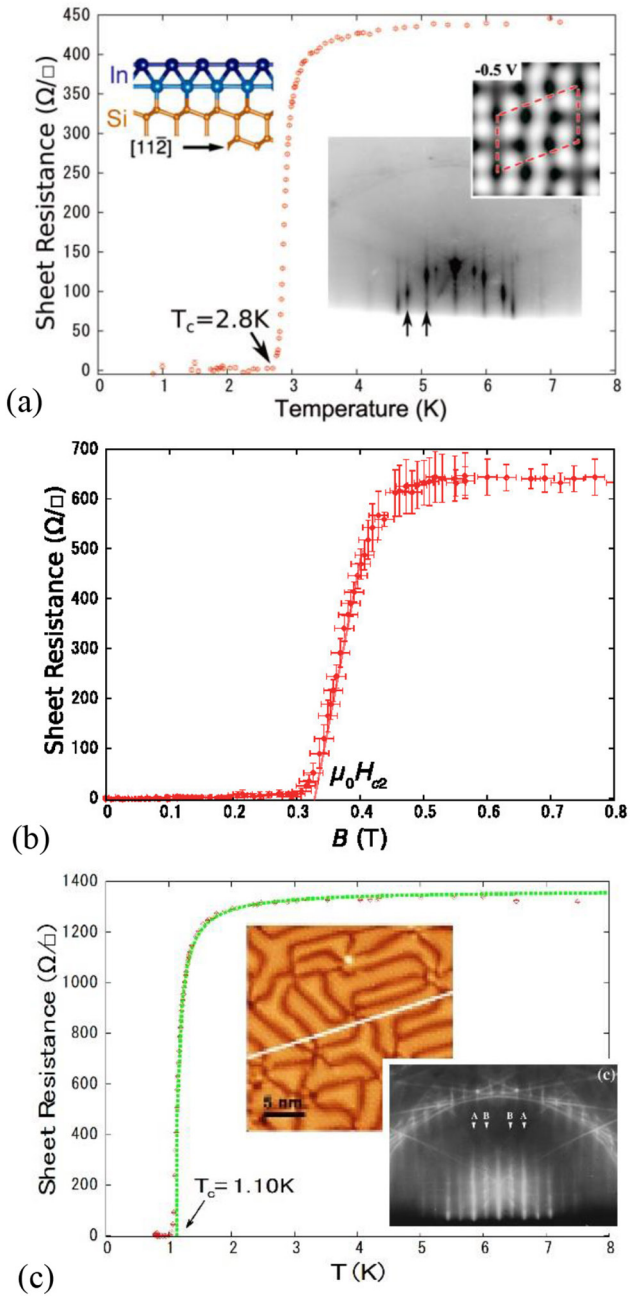

Figure 4. (a) Sheet resistance of Si(1 1 1)- $\sqrt{7} \times \sqrt{3}$-In surface superstructure at low temperature. Reprinted figure with permission from [37], © 2013 American Physical Society. The insets are RHEED pattern and structural model and simulated STM image taken from [40] with permission, © 2012 American Physical Society. (b) That of the same surface as a function of magnetic field applied perpendicular to the surface at $T = 0.8$ K [37]. (c) That of Si(1 1 1)-SIC-Pb surface superstructure. (b) adn (c) are reprinted with permission from [37], © 2013 American Physical Society. The insets are its STM image (from [34] © 2010 Macmillan Publishers Limited. All rights reserved. With permission of Springer) and RHEED pattern [38] (Reprinted with permission, © 1999 American Physical Society.).

and a striped incommensurate (SIC) phase are formed at less than 1.2 ML and more than 1.3 ML coverages, respectively. Both phases show superconducting gap opening below 2 K [34] detected by STS. Figure 4(c) shows the sheet resistivity of the SIC phase as a fucntion of temperature, showing

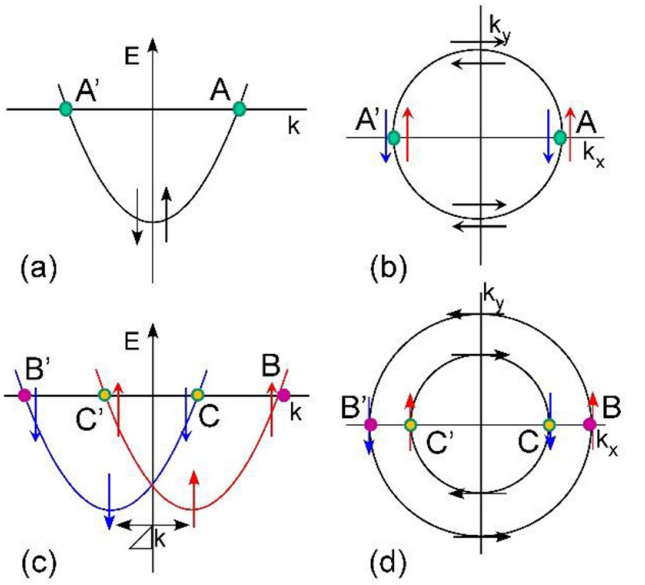

Figure 5. (a) Band dispersion and (b) Fermi surface of a spin-degenerate 2D electron gas (2DEG) system. (c) and (d) Those of a 2DEG with Rashba-type spin-splitting.

a superconducting transitoin at 1.1. K [37]. As in the case of Indium mentioned above, the coference length measured by magneic field application, indicates dirty superconductivity where the coherence length is limitted by the carrier mean free path.

4. Rashba superconductivity in surface states

Surface-state superconductivity can provide very interesting physics due to broken space-inversion symmetry at the crystal surfaces. So-called Rashba effect is induced by the broken symmetry and strong spin–orbit intercation, resulting in splitting in energy levels between spin-up electrons and spin-down electrons [41]. When such Rashba-type surface states become superconducting, we can expect unconventional superconductivity.

Let us consider first a 2D free-electron system having a parabolic band dispersion and a circular Fermi surface, as shown in figures 5(a) and (b), with space-inversion symmetry kept. For lack of Rashba effect in this case, electrons at points A nd A' on the Fermi level are spin-degenerate without splitting in energy and wavevector (Kramers degeneracy). As a result, they make quantum mechanical states with spin-up and spin-down electrons superpositioned each other, so that the Cooper pairs in the superconducting state (the orbital part of the wavefunction) are spin-singlet

$$|k_A\uparrow\rangle|-k_{A'}\downarrow\rangle - |k_A\downarrow\rangle|-k_{A'}\uparrow\rangle \tag{1}$$

or spin-triplet

$$\begin{aligned} &|k_A\uparrow\rangle|-k_{A'}\downarrow\rangle + |k_A\downarrow\rangle|-k_{A'}\uparrow\rangle, \\ &|k_A\uparrow\rangle|-k_{A'}\uparrow\rangle, \\ &|k_A\downarrow\rangle|-k_{A'}\downarrow\rangle, \end{aligned} \tag{2}$$

where $k_{A,\,A'}$ and $\uparrow\downarrow$ indicate the wavevector and spin of an electron at the Fermi level, respectively. By space-inversion

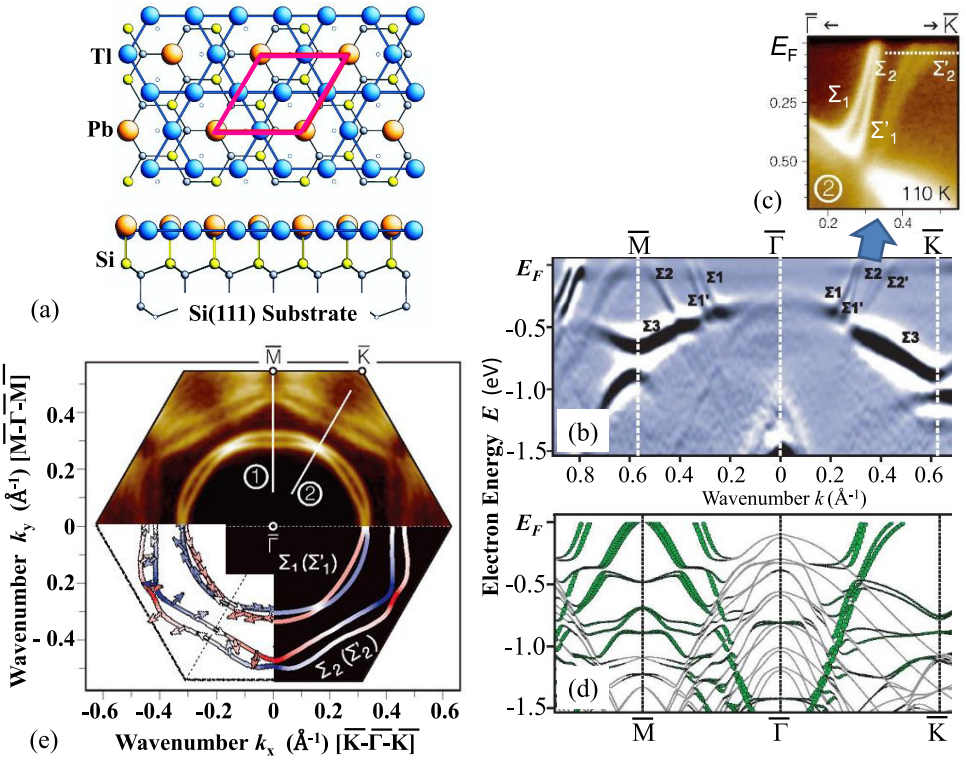

Figure 6. Si(1 1 1)- $\sqrt{3} \times \sqrt{3}$-(Pb+Tl) surface [47] (a) schematics of atomic arrangement. (b) Band dispersion measured by ARPES, and (c) its magnified figure. (d) Band dispersion calculated by the first-principles theory. Green lines show the surface-state bands. (e) Fermi surface measured by ARPES (upper half) and that calculated by the first-principles theoy (lower half). Small arrows indicate in-plane components of spin at Fermi level, while color of the lines indicate the out-of-plane component. Reproduced from [47], CC BY 3.0.

operation which reverse the momentum directoin ($k_A \Leftrightarrow -k_{A'}$), the spin-singlet wavefunction equation (1) changes the sign (odd-parity). On the other hand, the spin-triplet Cooper pairs equation (2) is even-parity; the space-inversion operqation does not change the state. In this way, we can classify the wavefucntion distinctly in terms of parity. This is due to the space-inversion symmetry. But, once the spcae-inversin symmetry is broken down to have Rashba effect and spin-split bands, as shown in figures 5(c) and (d), the electrons having opposite spin with the same wavevector are not on the same Fermi surface any more. As a result, the electrons at points B and B' (figures 5(c) and (d)) form a pair ($|k_B \uparrow\rangle\,|-k_{B'} \downarrow\rangle$), and the electrons at C and C' form a pair ($|k_C \downarrow\rangle\,|-k_{C'} \uparrow\rangle$) separately. Since these wavefunctions of pairs, however, are transformed by space-inversin operation ($k_B \Leftrightarrow -k_{B'}$) into states which are neither symmetric nor anti-symmetric with respect to the particle exchange in the initial states, these states are not allowed to exist. Therefore, by introducing an imaginary state $|k_B \downarrow\rangle\,|-k_{B'} \uparrow\rangle$ which is the space-inversted fucntion of the state $|k_B \uparrow\rangle\,|-k_{B'} \downarrow\rangle$ but not exist, for example, the Cooper pair of electrons at B and B' can be re-written as

$$\begin{aligned}&|k_B \uparrow\rangle\,|-k_{B'} \downarrow\rangle \\ &= \tfrac{1}{2}(|k_B \uparrow\rangle|-k_{B'} \downarrow\rangle - |k_B \downarrow\rangle|-k_{B'} \uparrow\rangle) + \tfrac{1}{2}(|k_B \uparrow\rangle|-k_{B'} \downarrow\rangle \\ &\quad + |k_B \downarrow\rangle|-k_{B'} \uparrow\rangle).\end{aligned} \tag{3}$$

Since the second and fourth term concel out each other, the introduction of these terms is mathematically allowed. The first and second terms look like a spin-singlet Cooper-pair wavefunction equation (1) which has odd parity, while the third and fourth terms look like a spin-triplet Cooper-pair wavefunctin equation (2) which is even-parity. Thus, the wavefunction of Cooper pairs in the spin-split bands is composed of mixtures of spin-singlet- and -triplet Cooper pairs. This is called 'parity-broken superconductivity'. This kind of unconventional superconductors are expected to have novel properties such as anormously large critical magnetic field [42] and to be topological superconductors as mentioend below. Since the Rashba spin-splitting is large in the systems composed of heavy elements like Pb due to strong spin–orbit coupling, these effects of the mixed Cooper pairs are expected in the Pb-induced surface structures [43, 44].

A surface-state superconductor is found which shows gigantic Rashba effect; it is a single atomic layer of Pb and Thallium (Tl) alloy on Si(1 1 1) [45, 46]. When we deposit 1 ML of Tl and 1/3 ML of Pb on Si(1 1 1) surface, a $\sqrt{3} \times \sqrt{3}$ superstructure is formed (figure 6(a)) [47]. ARPES exhibits the band dispersion as shown in figure 6(b), clearly showing dispersive metallic bands crossing the Fermi level in both of $\bar{\Gamma}$–$\bar{M}$ and $\bar{\Gamma}$–$\bar{K}$ directions. These are furthermore split into two, as shown in the magnified figure in figure 6(c). Figure 6(d) is the band dispersion obtained by the first-principle calculation based on the atomic arrangement shown in figure 6(a), which reproduces the ARPES result of figure 6(b) very well. The calculation shows that the spins of electrons in the two-fold bands point in opposite directions from each other. The energy splitting between the opposite-spin electrons at the same wavenumber is as large as 250 meV.

The upper half of figure 6(e) is the Fermi surface obtained by ARPES, while the lower half is calculated by the

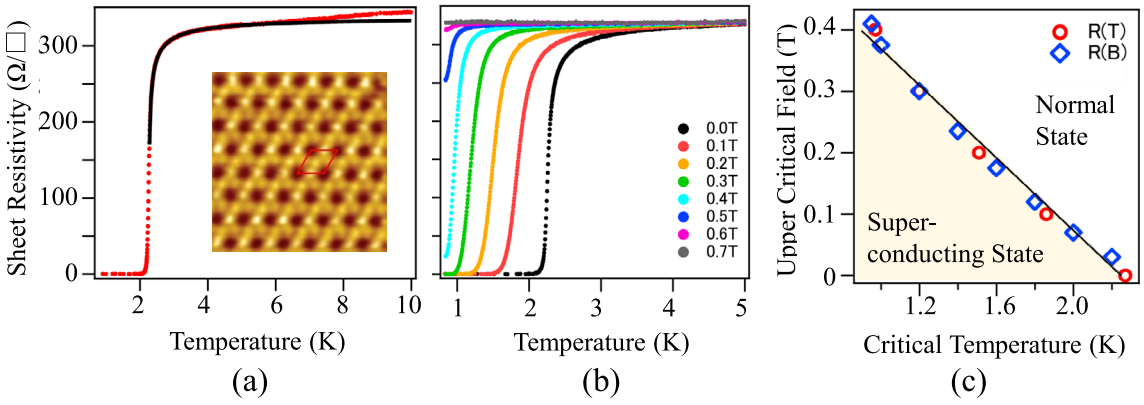

Figure 7. Surface-state superconductivity on Si(1 1 1)-$\sqrt{3} \times \sqrt{3}$-(Pb + Tl) surface [45]. (a) Temperature dependence of the sheet resistivity under zero magnetic field. A black line is a fitted result by Aslamazov–Larkin–Maki–Thompson theory for 2D superconductivity. (b) Temperature dependence of the sheet resistivity under surface-normal magnetic field. (c) A phase diagram for the relation between the critical temperature and the upper critical magnetic field. Reprinted figure with permission from [45], © 2015 American Physical Society.

first-principle method. We see circular Fermi surfaces and nearly hexagonal Fermi surfaces, both of which are split into two, respectively. This splitting corresponds to the split metallic bands in figures 6(b) and (c). Small arrows in the lower half on the Fermi surface indicate the in-plane spin components, showing that they are opposite each other between the split bands. These results clearly indicate that the surface states of this Si(1 1 1)-$\sqrt{3} \times \sqrt{3}$-(Pb+Tl) shows the Rashba effect. These surface states are Shockley states composed of the valence electrons of Pb and Tl atoms.

Figures 7(a) and (b) show the sheet resistivity of this surface at low temperature measured by monolithic 4PP (figure 1(e)) in UHV [45]. The results clearly show a superconducting transition around 2.3 K, and the surface-normal magnetic field makes the critical temperature (T_C) lower. A field of ca. 0.7 T totally suppresses the superconducting transition, corresponding to the upper critical field (H_{C2}). A phase diagram summarizing the relation between T_C and H_{C2}, shown in figure 7(c), gives us the Ginzburg–Landau coherence length ξ_{GL} as about 20 nm. Since this length is much longer than the thickness of one-atom layer, we can say that this system is a 2D superconductor. As in the In-atomic layer in figure 4, the gradual decrease in the sheet resistivity above T_C with cooling is due to superconducting fluctuation which is enhanced in 2D systems; the Cooper pairs are formed incoherently above T_C, which makes the resistance gradually lower, and the pairs become coherent to make the resistance zero at T_C. The current–voltage curves around T_C (not shown here) follow a characteristic power law, which is a sign of superconducting transition in 2D systems based on Berezinskii–Kosterlitz–Thouless theory [35]; creation and annihilation of pairs of vortex-anti-vortex and their dissociation are induced around T_C.

In addition to the two-dimensionality of this superconductivity, the spin-splitting due to the Rashba effect mentioned in figure 6 can make this system a parity-broken superconductor as described above [46]. Actually low-temperature STM and STS have revealed some signatures of the unconventional superconductivity in the structures of vortex cores and a pseudo-gap [46].

When the topological surface states transit to be superconducting, such 'topological superconductivity' should be also unconventional [48]. Topological superconductors, which can

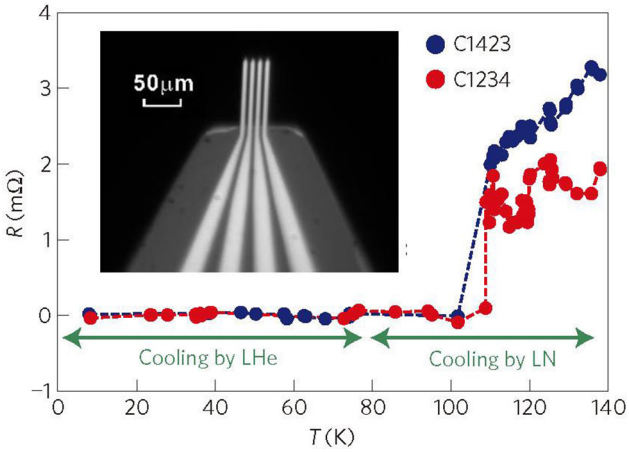

Figure 8. High-T_C superconductivity of a single-unit layer of FeSe grown on $SrTiO_3$ [49]. The inset is a micro-four- point probe attached on a low-temperature STM head. Reproduced from [49], © 2014 Macmillan Publishers Limited. All rights reserved. With permission of Springer.

be made with parity-broken superconductors or with junctions between topological insulators and superconductors, have energy gaps in the bulk (or in the central part of the surface/interface), while their edges/surfaces have gapless metallic states (Andreev bound states), much like at topological insulators. The edge/surface states are protected by 'bulk-edge correspondence'. It is predicted by theory that such edge states host Majorana states where 'particles' and 'anti-particles' are the same. This is a hot topic towards quantum computers where the calculation is based on manipulation of interacting Majorana states.

Another interesting result recently reported on the superconductivity at atomic layers is a single unit-cell film of FeSe epitaxially grown on $SrTiO_3$(0 0 1) substrate. This shows superconductivity above 100 K, reveal by *in situ* micro-4PP method in UHV (figure 8) [49]. This is a much higher T_C than that of bulk crystal (9.4 K). Although the electronic states of the substrate may contribute to enhancing the superconductivity of FeSe layer, the detailed mechanism for the high T_C is still under debate. 2D superconductivity including the surface-state superconductivity is now a hot topic in condensed matter physics.

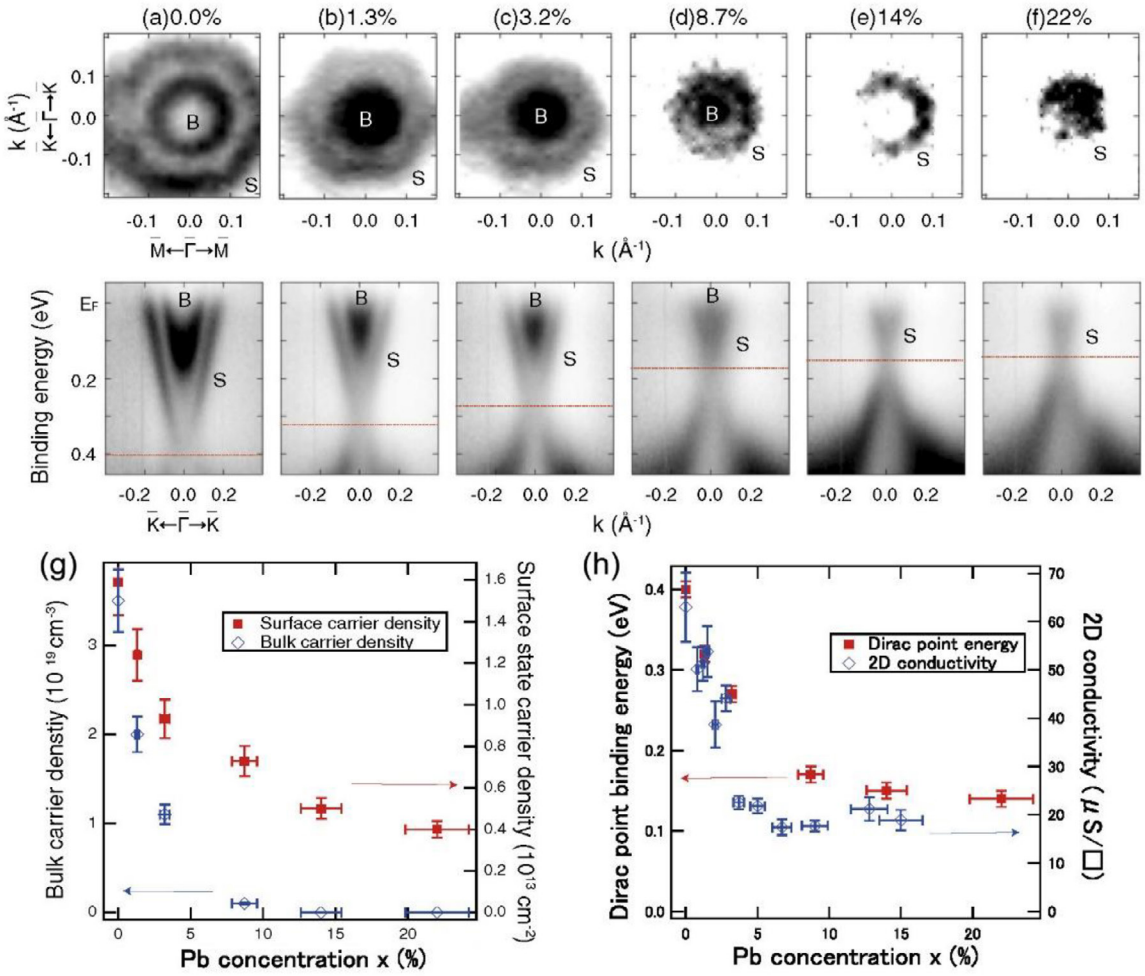

Figure 9. (a)–(f) Fermi surface (upper row) and band dispersion (lower row) of the Bi_2Te_3 thin films grown on Si(1 1 1) with a Pb doping concentration of 0 (a), 1.3 (b), 3.2 (c), 8.7 (d), 14 (e), and 22% (f), respectively. The horizontal lines in the band dispersion diagrams indicate the position of the Dirac point. B and S represent the bulk and surface states, respectively [50]. (g) Change in the bulk and surface-state carrier densities for the Bi_2Te_3 thin films doped with different Pb concentrations, calculated from area of the measured Fermi surfaces (a)–(f). (h) The change in the Dirac-point energy position (from (a)–(f)), together with the measured 2D sheet conductivity. Reproduced from [50]. Copyright © 2013 The Japan Society of Applied Physics.

5. Transport at topological surface states

When the spin–orbit interaction is strong enough in the broken space-inversion-symmetry systems, we have more than Rashba effect; so-called 'band inversion' occurs where the bottom of the conduction band and the top of the valence band are exhcnaged in energy potisition, resulting in topological insulators. This makes the bands 'twisted'; the parity changes partially within single bands, which is called 'topologically non-trivial'. Since the vacuum is a 'topologically trivial insulator in which such a 'band twist' does not occur, the surface of a topological insulator is the interface between the twisted-band insulator and the non-twisted-band insulator. Then, such a surface always hosts metalic surface-state bands which connect the conduction and valence bands of the bulk states by spanning the band gap. The topological surface states do not disapper unless the band inversion is resolved in the bulk bands. Therefore the surface states are robust againist defects and contaminations on the surfaces and not depend on the details of chemical bonds at surface atomic layers. This is because, as mentioned above, the surface states originate from the bulk band inversion, not from the surface properties. This distinctly contrasts to the nature of traditional Shockley/Tamm-type surface states [41]. Although the topological surface states never disappear, they can be degreaded in the properties by defects and contaminatoin.

Well-known examples of 3D topological insulators are Bi_2Se_3 and Bi_2Te_3, of which surface states are spin-split with Dirac-cone-type linear dispersion. Since the Fermi surface of the topological surface states has a so-called spin texture structure, 'spin-momentum locking' effect occurs; the spin of electrons is always perpendicular to the direction of current flow. Therefore, some kinds of spin-related transport are expected. But, in many of real crystals of topological insulators, the bulk states are not really insulating due to many defects in the crystals. Therefore, the electrical curent flows through the bulk states as well as the metallic surface states. Then, we need to make the bulk states insulating for detecting the transport properties of the topological surface states.

Figure 9(a) shows ARPES results of the Fermi surface (upper pannels) and the band dispersion near the Fermi level E_F around $\bar{\Gamma}$ point (lower pannels) taken from an ultrathin film

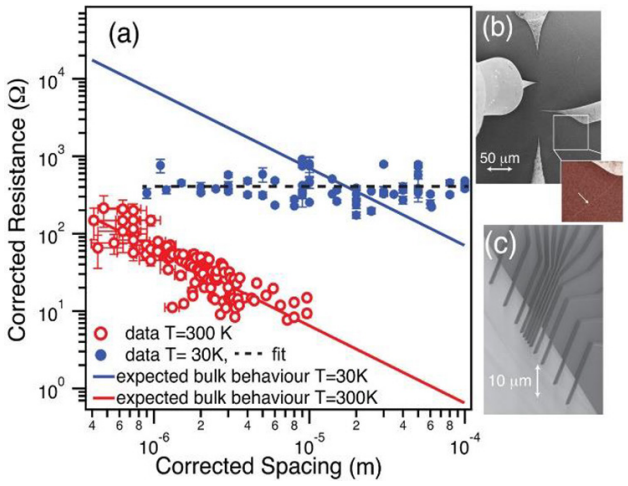

Figure 10. Four-point-probe resistance measurements on a clean Bi_2Te_2Se surface taken at 300 K (open circles) and at 30 K (filled circles), together with the expected result for bulk dominated transport at these two temperatures (solid lines) [52]. (b) Scanning electron microscopy (SEM) image of the four-tip STM contacts used for the 30 K measurements. (c) SEM image of the 12-point probe for the 300 K measurements.

of Bi_2Te_3 grown on Si(1 1 1) substrate [50]. We can see that the bulk conduction band denoted by *B* as well as the Dirac-cone-type surface states denoted by *S* cross E_F. This means the inside of the film is a degenerated *n*-type semiconductor, due to Te deficits, which enhances the electrical conductivity through the interior of the film. In order to make the current flow preferentially through the surface states, the bottom of the bulk conduction band should be abobe E_F, so that E_F crosses the surface state bands only. For it, Pb atoms were incorporated during the grwoth of Bi_2Te_3 film because Pb atoms are expected to replace Bi sites, resulting in hole doping in the film. Actually, as shown in figures 9(b)–(f), the whole bands are raised in energy position with increasing the Pb concentration, and 14% concentration of Pb is enough to raise the conduction-band bottom above E_F and the Fermi surface of the conduction band disappears (figure 9(e)). Accordingly, the bulk carrier density, calculated from the area of the Fermi circule *B*, decareses and finally disappears with the Pb cncentration, as shown in figure 9(g), while the surface-state carrier density remains because E_F crosses the surface bands S only.

The sheet (2D) conductivity measured *in situ* by monolithic micro-4PP (figure 1(e)) in UHV decreases with the Pb doping as shown in figure 9(h), which is consistent with the decreases in the carrier densities in figure 9(g), and saturates around 20 μS at around 14% Pb concentration. This value corresponds to the conductivity by the Dirac-cone type topological surface states because the bulk bands are above E_F as mentioned above. From this value of conductivity, together with the carrier density in the surface states (calculated from the area of the Fermi surface *S*), the carrier mobility is calculated to be around 30 $cm^2\,V^{-1}\,s^{-1}$ by using the Drude formula. This value of mobility is about twice of that of a non-topological surface state of Si(1 1 1)-$\sqrt{3}\times\sqrt{3}$-Ag surface [51]. This is disappointing because the carrier mobility in the Dirac-cone-type topological surface states is naively believed to be very high bacuse of supression of back scattering in the topological surface states. But this is not true for 2D surface states; although 180° backscattering of carriers in the topological surface states is prohibited due to spin-momentum locking, backscattering at other angles are allowed at e.g. domain boundaries, atomic steps and point defects, as shown by STP [23, 24] in figure 2, which makes the carrier mobility lower.

Another example is shown in figure 10 where the surface-state transport of a topological crystal Bi_2Te_2Se is directly measured by using a twelve-point probe shown in figure 1(f) and four-tip STM [52]. Bi_2Te_2Se is a topological insulator with highly insulating bulk states where E_F is located within the bulk band gap so that only the surface states cross E_F. After cleaving the bulk crystal in UHV, 4PP resistance measurements were done *in situ* by choosing four probes out of the twelve probes and also by using four-tip STM to obatined the probe-spacing dependence of the resistance. The twelve-point probe enables measuring the resistance with different probe spacings just by choosing different combinatoins of four probes out of the twele probes, while the tips are re-positioned in the four-tip STM for 4PP measurements with different probe spacings. Figure 10 shows the resistance as a fucntion of the effective probe spacing ranging from 400 nm to 100 μm [52]. The resistance at 300 K is inversely proportional to the probe spacing, while it is almost constant independent of the spacing at 30 K. This means different dimensionalities in the transport; the resistance for a 2D sheet R_{2D} and that for a 3D bulk R_{3D} have different dependences upon the probe spacing *d*;

$$R_{2D} = \frac{\ln 2}{2\pi} R_S,\ R_{3D} = \frac{\rho}{2\pi d}, \tag{4}$$

respectively, by assuming that the *d* is much smaller than the size of the samples [4, 53]. Here R_S is the sheet resistivity ($\Omega/\square$) and ρ is the 3D resistivity ($\Omega\cdot$ cm). Then the results in figure 10 indicate that the measurement current flows through the bulk states inside the crystal at 300 K, showing 3D conduction, while the bulk carriers are frozen out at 30 K and the current flows through the metallic surface states only, showing 2D conduction. From the area of Fermi circle of the Dirac-cone type surface state measured by ARPES, the carrier density is calculated. Then by combining the conductivity derived from figure 10, we can deduce the carrier mobilityto be about 390 $cm^2\,V^{-1}\,s^{-1}$. This value is higher than that of the surface states of Pb-doped Bi_2Te_3 in figure 9 by one order of magnitude. This may be because the doped Pb atoms act as carrier scatterers to reduce the carrier mobility in figure 9.

The temperature dependence of resistivity in the Dirc-cone type surface state on Bi_2Te_3 is directly measured *in situ* by macroscopic four-terminal method in UHV as shown in figure 11 [54]. The authors of this paper claimed that defects in the epitaxial Bi_2Te_3 film were reduced by optimizing the growth condition so that the inside of the film could be insulating without any doping, which was confirmed by ARPES (figure 11(a)). The sheet resisitviity shows a metallic behavior as shown in figure 11(b) where the resisitvity decreases with cooling. This does not come from the insulatung bulk states, but from the metallic Dirac-cone type surface states. By the same procedue as before to obtain the carrier density from ARPES data, the carrier mobility in the surface state is

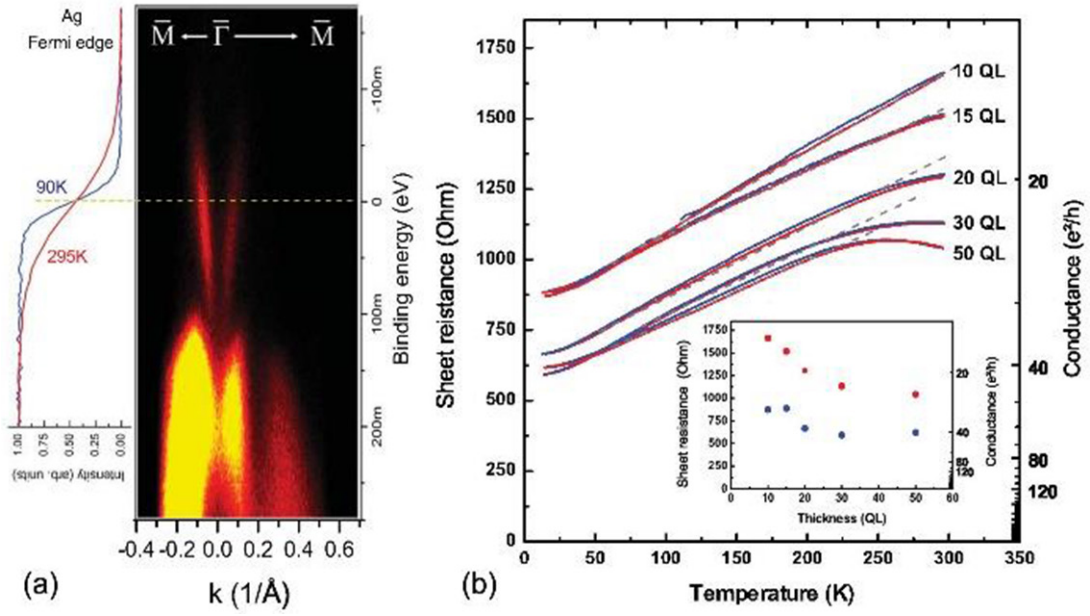

Figure 11. (a) Band dispersion of a 10 quintuple layer (QL) thick film of Bi_2Te_3 measured at room temperature. (b) Temperature-dependent sheet resistance of thin Bi_2Te_2 films of different thicknesses (from 10 to 50 QL thick) measured *in situ* in UHV [54].

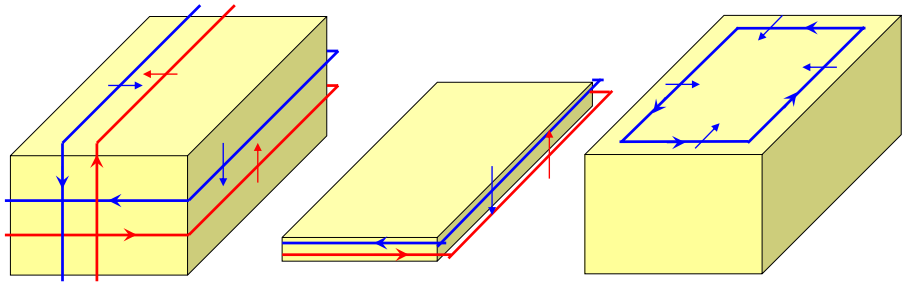

(a) 3D TI (b) 2D TI (c) 3D Magnetic TI

Figure 12. Spin-polarized currents (a) on the surfaces of a 3D topological insulator and (b) at the edge of a 2D topological insulator (helical edge state), and (c) at the chiral edge state on a magnetic topological insulator.

estimated to be 4600 $cm^2\ V^{-1}\ s^{-1}$. This is much higher than those in the previous results, which is considered to originate from the high quaity of sample and clean surface [54]. This high mobility may be intrinsic to the topological surface states.

These studies have illustrated that the electrical conductivity through the topological surface states can be detected by suppressing the bulk conductivity by making the bulk insulating, and that the characteristics intrinsic to the topological surface states depend on or even hampered by the defects and poor quality of samples.

6. Spin transport at surfaces

Bismuth is a non-topological material (a trivial material) having Rashba-type spin-split surface states that are Shockley/Tamm type [41], so that they are easily destroyed by defects and contaminations on the surface. Since, however, both of topologcal surface states and Rashba-type surface states have spin-split metallic bands and spin texture structures on the Fermi surfaces, we can expect spin-polarized current flowing on the both types of surfaces.

Spin-resolved transport measurements are a new challenge in the surface-state transport physics. Due to spin texture structures on the Fermi surfaces of Rashba-type and topological surface states, so-called 'spin-momentum locking' occurs where the spin of an conduction electron is always perpendicular to its momentum, resulting in spin-polarized current flowing on the surfaces (figure 12). For an example, when the unpolarized curent is injected into a sample from a non-magnetic tip, as shwon by a Pt tip (tip 3) in figure 13(a), the current flows out isotropically on the sample surface. The spins of conduction electrons are indicated by small red arrows which are perpendicular to the current directions (long blue arrows). In order to detect this spin-polarized current in a particular direction, a magnetic tip (CoFe-coated carbon nanotube tip, tip 1 in figure 13) was used to measure the voltage drop between the electrode for reference (W tip, indicated by tip 2 in figure 13(a)) [25]. The measured voltage should be different depending on whether the magnetization direction of CoFe tip and spin direction of the current are parallel or anti-parallel to each other, because the chemical potenteials for the majority and minority spins in the magnetic tip are different in energy so that the contact voltage between the CoFe tip and sample

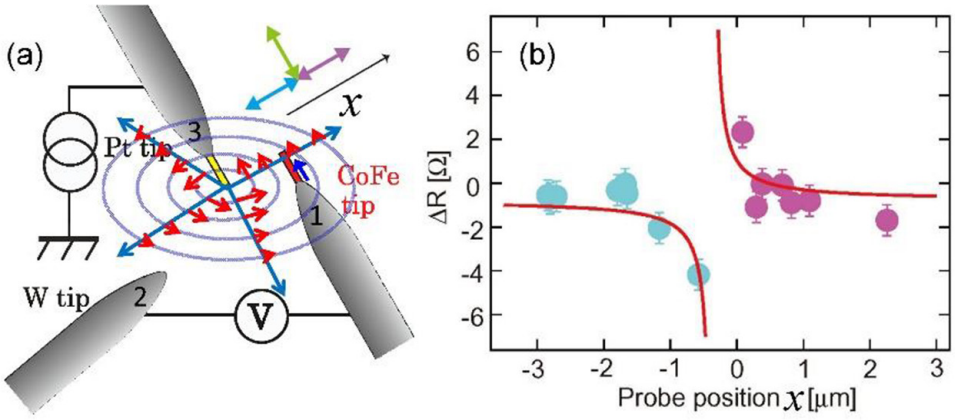

Figure 13. (a) Schematic drawing of the multi-tip STM measurement for spin-polarized current. The spin-dependent potential, induced by the current injected from the Pt-coated CNT tip (3) into the Bi film was measured by the CoFe-coated CNT tip (1). The (blue) arrows show the current flowing out from the Pt tip. The short (red) arrows show the induced spin polarization. (b) Deviation of resistance due to break down of Onsager's reciprocity relation, as a function of the distance between the Pt and CoFe tips [25].

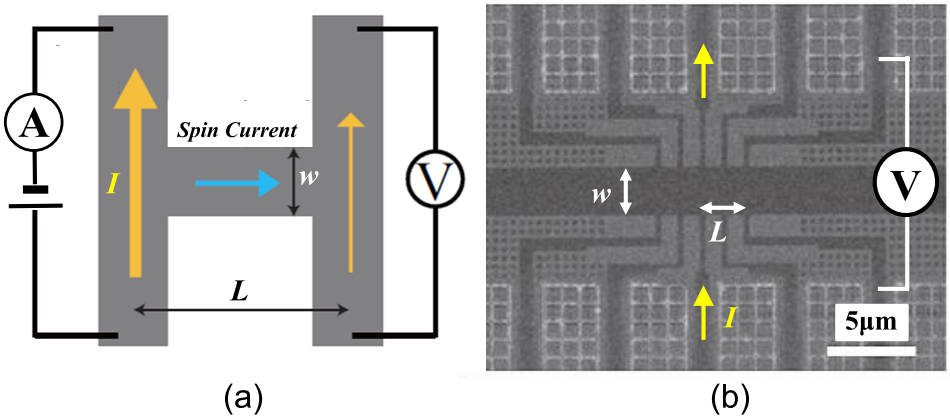

Figure 14. (a) Schematic drawing of a sample pattern and configuration for spin-Hall effect experiment, and (b) an example of sample for it; a focused-ion-beam-fabricated pattern out of a Bi_2Se_3 ultrathin film on Si substrate in UHV [56].

should differ depending on the spin-polarization direction of the current. Because of this effect, the measured resistance that is the voltage between the CoFe tip and W tip devided by the inject current from the Pt tip, should deviate from Ohm's law (and Onsager's recirocal relation). This deviation in resistance ΔR was measured at different positoins of the CoFe tip while the other tips were fixed. Figure 13(b) shows the measured ΔR as a function of the distance x between the magnetic CoFe tip and the current injection Pt tip [25]. The postive side of the horizontal axis means that the CoFe tip is on the right side of the Pt tip, while the negative side of the axis means the opposite location of the CoFe tip with respect to the Pt tip. At the distance over 1 μm, ΔR is almost zero, while at distance samller than 1 μm, ΔR is non-zero values with opposite sign between $+x$ side and $-x$ side.This is because, as illustrated in figure 13(a), the spin direction is opposite to each other in $+x$ and $-x$ directoins, and such spin-polarization survives only around 1 μm. This inidcates a sign of detection of spin-polarized current.

An interesting phenomenon called 'spin-Hall effect' occurs on the surface of a material having strong spin–orbit interaction [55]. When an electrical current flows along y direction, flow of up-spin electrons in the current is bent to e.g. $+x$ direction, while flow of down-spin electrons is bent to $-x$ direction. This occurs without external magnetic field, because the imaginary magnetic field caused by the strong spin–orbit interaction is built in on the surface. Since the unpolarized current along y direction contains the same number of up-spin electrons and down-spin electrons, this phenomenon does not produce any electrinic current in x-direction, but make a flow of angular momentum; a net flow of the angular momentum corresponding to up-spin occurs in $+x$ direction. In other words, there is no charge current in x direction, but a so-called 'pure spin current' flows in this direction which is perpendicular to the original electrical current.

For an example, in a H-shape structure shown in figure 14(a), when an electrical current flows along the left-side branch, the spin current flows along the horizontal bridge due to the spin-Hall effect mentioned above. A time-reversal process of the spin Hall effect occurs at the right side of the bridge (inverse spin Hall effect); the pure spin current produces an electrical current flowing along the right-side branch, resulting in a volatge appearing on the right-side branch. In other words, information can be transmitted from the left side to the right side through pure spin current. Since the pure spin current does not accompany charge flow by definition, in principle no Joule heating occurs at the bridge part in figure 14(a); the information is transmitted without energy dissipation. This opens up an interesting expectation for

ultralow energy-consumption devices by using spin current. Figure 14(b) is an example of such a device, fabricated by focussed ion beam in UHV combined with four-tip STM system [56]. The electric current I is made flow through leads at the center and the voltage V is measured between leads apart from the current leads by distance L; the spin current is expected to flow along the horizontal strip of a topologocal insultor. The results will be published elsewhere.

7. Concluding remarks

In this short review, we have discussed trasnport phnomena at 2D electronic systems on the surfaces of 3D crystals. An interesting direction for further study may be 'edges of surfaces'. In 2D topological insulators, edge states appear in which spin-polarized current flows (figure 12(b)). This is called helical edge states with time-reversal symmetry kept. Furthermore, because of prohibition of 180° backscattering there, the flow should be dissipation-less (quantum spin Hall effect) [57]. Some kinds of materials are proposed to be 2D topological insulators [58–60]. Similar, but time-reversal-symmetry-broken edge states (chiral edge states) appear by introducing magnetic order in the topological surface states (figure 12(c)). This shows again dissipation-less transport, called quantum anormalous Hall effect. This is already confirmed experimentally at low temperatures [61].

A new idea comes out about the edge states, so-called 'hinge states' of higher-order topological insulators in which symmtery in crystal structures are a key for topological protection [62, 63]. These edges states are expected to be a platform for future devices of ultra-low energy comsumption and error-tolerant operation. The experimental techniques introduced here may be useful to characterize such 'edge-state trasnport', too.

Acknowledgment

I would like to acknowledge past and present members in my research group and also collaborators outside, too many to list here, for their contributions to some of the results presented here. I acknowledge also financial support from the Japan Society of Promotion of Science (KAKENHI 15H02105, 16H02108, 25246025, 22246006), Japan-Russia Bilateral Program, and MEXT for Grant-in-Aid for Scientific Research on Innovative Areas 'Molecular Architectonics' (No. 25110010).

ORCID iDs

Shuji Hasegawa https://orcid.org/0000-0002-6324-0525

References

[1] Hasegawa S *et al* 1999 *Prog. Surf. Sci.* **60** 89
Hasegawa S *et al* 2003 *Surf. Rev. Lett.* **10** 963
[2] Miccoli I *et al* 2015 *J. Phys.: Condens. Matter* **27** 223201
[3] Voigtlander B *et al* 2018 *Rev. Sci. Instrum.* **89** 101101
[4] Ph Hofmann and Wells J W 2009 *J. Phys.: Condens. Matter* **21** 013003
[5] Ji S-H *et al* 2012 *Nat. Mater.* **11** 114
[6] Baringhaus J *et al* 2014 *Nature* **506** 349
[7] Barreto L *et al* 2013 *Appl. Phys. Lett.* **102** 033110
[8] Ichinokura S *et al* 2016 *ACS Nano* **10** 2761
[9] Jentzsch F *et al* 1989 *J. Appl. Phys.* **66** 5901
[10] Hasegawa S and Ino S 1992 *Phys. Rev. Lett.* **68** 1192
[11] Uchihashi T, Mishra P and Nakayama T 2013 *Nanoscale Res. Lett.* **8** 167
[12] Shiraki I *et al* 2000 *Surf. Rev. Lett.* **7** 533
[13] Okamoto T *et al* 2011 *J. Appl. Phys.* **109** 102416
[14] Henzler M and Heiland G 1966 *Solid State Commun.* **4** 499
[15] Perkins E *et al* 2013 *Rev. Sci. Instrum.* **84** 033901
[16] Yoshimoto S *et al* 2007 *Nano Lett.* **7** 956
[17] Kanagawa T *et al* 2003 *Phys. Rev. Lett.* **91** 036805
[18] Yamada M *et al* 2012 *e-J. Surf. Sci. Nanotechnol.* **10** 400
[19] Pfnuer H, Luekermann D and Tegenkamp C 2012 *Phys. Status Solidi* a **209** 627
[20] Bannani A, Bobisch C A and Möller R 2008 *Rev. Sci. Instrum.* **79** 083704
[21] Homoth J *et al* 2009 *Nano Lett.* **9** 1588
[22] Nakamura T *et al* 2016 *e-J. Surf. Sci. Nanotechnol.* **14** 216
[23] Lüpke F *et al* 2017 *Nat. Commun.* **8** 15704
[24] Bauer S and Bobisch C A 2016 *Nat. Commun.* **7** 11381
[25] Tono T *et al* 2013 *New J. Phys.* **15** 105018
[26] Hus S M *et al* 2017 *Phys. Rev. Lett.* **119** 137202
[27] Chukurov E N *et al* 2012 *Surf. Sci.* **606** 191
[28] Abukawa T *et al* 1995 *Surf. Sci.* **325** 33
[29] Yeom H W *et al* 1999 *Phys. Rev. Lett.* **82** 4898
[30] Rotenberg E *et al* 2003 *Phys. Rev. Lett.* **91** 246404
[31] Yamazaki S *et al* 2011 *Phys. Rev. Lett.* **106** 116802
[32] Tanikawa T *et al* 2003 *e-J. Surf. Sci. Nanotechnol.* **1** 50
[33] Tanikawa T 2004 *Phys. Rev. Lett.* **93** 016801
[34] Zhang T *et al* 2010 *Nat. Phys.* **6** 104
[35] Berezinskii V L 1970 *Zh. Eksp. Teor. Fiz.* **59** 907 (1971 S*ov. Phys. JETP* **32** 493)
Kosterlitz J M and Thouless D J 1973 *J. Phys.* C **6** 1181
[36] Uchihashi T *et al* 2011 *Phys. Rev. Lett.* **107** 207001
[37] Yamada M *et al* 2013 *Phys. Rev. Lett.* **110** 237001
[38] Horikoshi K *et al* 1999 *Phys. Rev.* B **60** 13287
[39] Huoalo M *et al* 2003 *Phys. Rev. Lett.* **90** 216106
[40] Park J W *et al* 2012 *Phys. Rev. Lett.* **109** 166102
[41] Hirahara T *et al* 2007 *Phys. Rev.* B **76** 153305
[42] Sekihara T *et al* 2013 *Phys. Rev. Lett.* **111** 057005
[43] Sekihara T *et al* 2015 *J. Phys. Soc. Japan* **84** 064710
[44] Nam H-D *et al* 2016 *Proc. Natl. Acad. Sci. USA* **113** 10513
[45] Matetskiy A V *et al* 2015 *Phys. Rev. Lett.* **115** 147003
[46] Nakamura T *et al* 2018 *Phys. Rev.* B **98** 134505
[47] Gruznev D V *et al* 2014 *Sci. Rep.* **4** 4742
[48] Sato M and Ando Y 2017 *Rep. Prog. Phys.* **80** 076501
[49] Ge J-F *et al* 2015 *Nat. Mater.* **14** 285
[50] Aitani M *et al* 2013 *Japan. J. Appl. Phys.* **52** 110112
[51] Nakajima Y *et al* 1997 *Phys. Rev.* B **56** 6782
[52] Barreto L *et al* 2014 *Nano Lett.* **14** 3755
[53] Hasegawa S *et al* 2002 *Curr. Appl. Phys.* **2** 465
Shiraki I *et al* 2001 *Surf. Sci.* **493** 633
[54] Hoefer K *et al* 2014 *Proc. Natl Acad. Sci. USA* **111** 14979
[55] Murakami S *et al* 2003 *Science* **301** 1348
Ando Y 2013 *J. Phys. Soc. Japn* **82** 102001
[56] Fukui N *et al* 2014 *e-J. Surf. Sci. Nanotechnol.* **12** 423
[57] Koenig M *et al* 2007 *Science* **318** 766
[58] Murakami S 2006 *Phys. Rev. Lett.* **97** 236805
[59] Hirahara T *et al* 2011 *Phys. Rev. Lett.* **107** 166801
[60] Sakamoto R *et al* 2014 *J. Am. Chem. Soc.* **136** 14357
[61] Chang C-Z *et al* 2013 *Science* **340** 167
[62] Schindler F *et al* 2018 *Nat. Phys.* **14** 918
[63] Fruchart M 2018 *Nature* **555** 318